Impact parameter dependence of preequilibrium particle emission

D. Prindle, R. Vandenbosch, S. Kailas,* A. Charlop, and C. Hyde-Wright
University of Washington, Nuclear Physics Laboratory GL-10, Seattle, Washington 98195
(Received 16 November 1992)

The energy spectra and angular distributions of protons, deuterons, tritons, and alpha particles from 215 MeV ^{16}O bombardment of Tb, Ta, and Au have been measured in coincidence with both evaporation residues and fission fragments. The evaporation residue and fission fragment triggers together with the angular momentum dependence of the evaporation residue-fission competition have enabled us to extract the impact parameter dependence of the light charged particle preequilibrium multiplicities within the fusionlike impact parameter domain. The light charged particle spectra can be parametrized as originating from a source with approximately 1/2 to 2/3 of the beam velocity and with a slope parameter of ~5–7 MeV. The proton multiplicities increase with decreasing impact parameter, in agreement with a nucleon exchange transport model prediction. The ratio of the complex particle to proton multiplicities decrease with decreasing impact parameter, suggesting dynamical effects in the complex particle production mechanism.

PACS number(s): 25.70.−z, 25.70.Jj, 25.70.Pq

I. INTRODUCTION

A nonequilibrium component is observed in the energy spectra and angular distributions of neutrons and light charged particles in heavy ion induced reactions. These particles are forward peaked and exhibit energy spectra extending to considerably higher energies than those corresponding to the velocity of the projectile. The multiplicity of these particles increases with increasing bombarding energy [1, 2] and may eventually play an important role in limiting the amount of energy which can be deposited in a composite system. For the most peripheral reactions some energetic forward-peaked particles can arise from sequential decay of projectilelike fragments [5, 3, 4, 6, 7]. Our interest in this study, however, concerns the preequilibrium particles emitted on the shorter time scale of the nuclear collisions. These particles are sometimes referred to as promptly emitted particles [8].

We now have a fairly complete understanding of the mechanism for preequilibrium *nucleon* emission in heavy ion reactions at bombarding energies per nucleon up to about the Fermi energy [8–13]. A semiquantitative understanding of the energy spectrum, angular distribution, and absolute multiplicities has emerged by considering a nucleon exchange model where the velocity from Fermi motion in the donor nucleus is coupled to the relative motion of the projectile and target. A quantitative understanding of the angular distribution requires incorporation of nucleon-nucleon scattering in the target nucleus as projectile nucleons traverse through it.

These considerations are not easily extended to complex particles such as d, t, and α particles and it is not clear whether the same mechanism and the *same impact parameter dependence* will hold for preequilibrium *nucleon* and preequilibrium *complex* particles. There is a hint that the impact parameter dependence is very different for protons and for alpha particles from the work of Awes *et al.* [14], who were able to measure the multiplicities separately for the two classes of events corresponding to full and small momenta transfers. These two classes of events correspond to fusionlike and quasielastic processes.

The delineation of impact parameters within the class of fusionlike processes is a difficult experimental challenge, especially for moderate bombarding energies. Tsang *et al.* [15] have calculated the dependence of a number of observables on impact parameter in intermediate energy heavy-ion reactions. They find that the mean multiplicity of fast nucleons and the linear momentum transferred to the target residue are relatively insensitive to the impact parameter at small impact parameters and incident energies below $E/A \leq 60$ MeV. Methods based on the velocity of the evaporation residue or on the average parallel velocity of detected particles [16] are particularly dangerous when applied to the study of preequilibrium particle emission as (spurious) kinematic correlations due to energy and momentum conservation may dominate over the impact parameter dependence of interest.

We report here an experiment to further define the impact parameter within the class of nearly full momentum transfer (fusionlike processes) by exploiting the angular momentum dependence of fission competition with neutron evaporation. Depending on the fissionability of the composite system, the division of the fusionlike events into the more and less central events can be accomplished by tagging on the evaporation residues and on the fission fragments. Statistical model calculations show that the diffuseness of the ℓ dependence of the fission-evaporation residue competition is not prohibitively large, and that

*Present address: Bhabha Atomic Research Centre, Bombay, India.

the dividing ℓ can be moved throughout the fusion range by a modest variation in the target Z and A. The target fissionability is kept sufficiently small that sequential fission following inelastic and transfer reactions is small.

The dependence of the reaction process on orbital angular momentum (impact parameter) for fusionlike reactions is illustrated in Fig. 1. The smallest impact parameters lead to fusion followed by particle evaporation while larger impact parameters lead to fusion followed by fission. Still larger impact parameters lead to peripheral processes (not shown) and are not studied in this experiment. Our experiment involves the measurement of light charged particles in coincidence with either fission fragments (FF) or evaporation residues (ER).

The organization of this paper is as follows. In Sec. II we discuss the experimental method and detectors. In Sec. III we give the relevant fusion cross sections and average impact parameters for FF and ER tags. We discuss the moving source parametrization used to describe the light particles in Sec. IV and give the results of moving source fits to the data in Sec. V. Finally, in Secs. VI and VII we discuss and summarize the experimental results and draw conclusions.

II. EXPERIMENTAL METHOD

In the experiments reported here we used the University of Washington superconducting booster to produce a beam of ^{16}O incident on targets of $^{159}_{65}$Tb, $^{181}_{73}$Ta, $^{nat}_{77}$Ir, and $^{197}_{79}$Au. The target thicknesses were 1.5 mg/cm^2, 600 μg/cm^2, 400 μg/cm^2, and 700 μg/cm^2, respectively. Fusion events followed by fission are detected when one of the fission fragments enters a surface barrier detector at back angles. Fusion events in which the compound nucleus only evaporates light particles are detected by a surface barrier telescope at small angles. Light charged particles (LCP) in coincidence with either of these tags are detected by an array of phoswich counters covering angles from 7° to 62°. Coincidence measurements were performed with a 215-MeV ^{16}O beam. The absolute fission cross sections were measured in a separate experiment using a 224-MeV ^{16}O beam.

A. Light charged particle detection

An array of 12 phoswich detectors was used for p, d, t, and He detection. A detailed description of our phoswich array is given in Appendix A. A short summary is given here.

A phoswich detector consists of a thin scintillator acting as a δE counter attached to a thicker scintillator acting as an energy counter, both viewed by a single photomultiplier tube attached to the back. The two scintillators have different decay constants for light output, allowing one to infer δE and E from the shape and amplitude of the output which in turn allows one to identify particle types. A plot of δE (fast) versus E (slow) is shown in Fig. 2. The fast plastic also allows an accurate time-of-flight (TOF) measurement. The TOF measurement is necessary when requiring a coincidence between a phoswich counter and either a fission fragment (FF) or evaporation residue (ER) tag. The TOF measurement also helps to separate $Z = 1$ isotopes in the phoswich counters.

An individual detector presents a square face to a

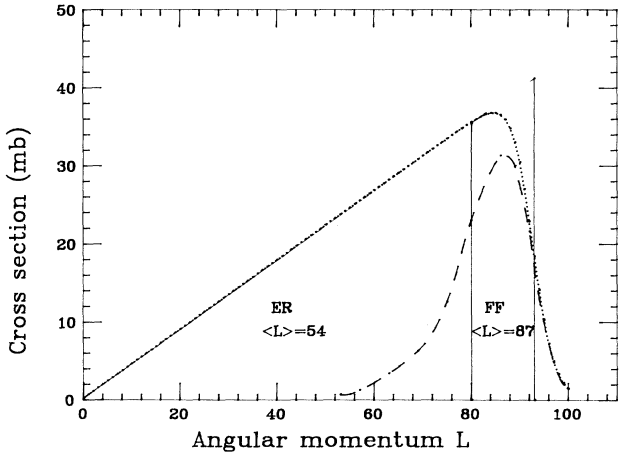

FIG. 1. Fusion cross section as a function of impact parameter for ^{159}Tb. The smallest impact parameters lead to fusion followed by particle evaporation (ER). Larger impact parameters lead to fusion followed by fission (FF). The solid curves are based on a sharp cutoff model and the cross sections in Table I. The dotted curve is for a smooth cutoff fusion distribution and the dashed curve gives a statistical model prediction of the diffuseness of the angular momentum dependence of the fission-evaporation residue competition.

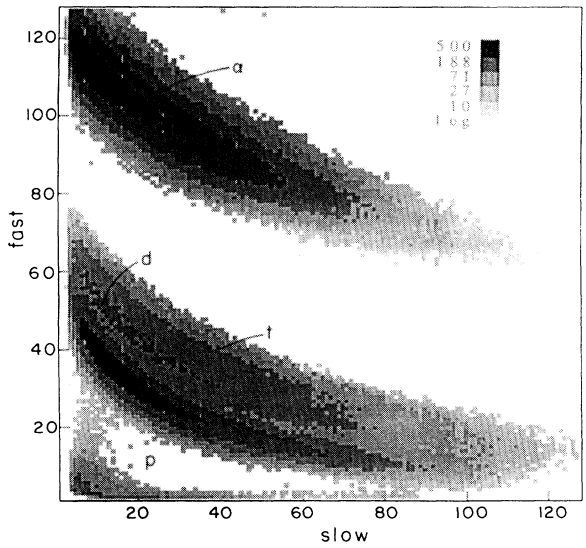

FIG. 2. δE vs E. "Fast" (dE) component of phoswich signal is vertical axis and "slow" (E) component of phoswich signal is horizontal axis. The gradation of the grey scale is logarithmic. The measured ADC values have been corrected for pedestals and then scaled to a uniform PMT gain. See Sec. III A for more details on the scaling.

particle coming from the target, with each edge of the counter covering an angle of about 7°. For the current experiment we placed eight counters in the reaction plane, with the centers of the counters ranging from 7° to 62°. We placed four counters out of the reaction plane at angles from 7° to 20°. The minimum energy to make it through the thin scintillator (so particle identification is possible) is 6 MeV for protons and 24 MeV for alphas. The energy to punch through the thick scintillator is about 55 MeV for protons and 220 MeV for alphas.

The detectors closest to the beam were subject to a large flux of scattered beam. To reduce pile-up problems these detectors were covered with a 0.125-mm Ta shield. This was thick enough to range out the beam, but thin enough so the particle identification thresholds were only slightly raised, to about 9 MeV for protons and 35 MeV for alphas.

We are able to cleanly separate $Z = 1$ and $Z = 2$. We do this by taking the difference between the measured fast component and the expected fast component calculated from the slow component. $\Delta_{\rm fast} = C_{\rm fast}^{\rm meas} - C_{\rm fast}(C_{\rm slow}^{\rm meas})$. Here C is the charge measured by the ADC. Separation of the $Z = 1$ isotopes is more difficult, and there we use a combination of $\Delta_{\rm fast}$ and $\Delta_{\rm TOF}$, where $\Delta_{\rm TOF} = {\rm TOF}^{\rm meas} - {\rm TOF}(C_{\rm slow}^{\rm meas})$ is the difference between the measured time of flight and the time of flight expected based on the slow light component. The plot of $\Delta_{\rm fast}$ versus $\Delta_{\rm TOF}$ for the $Z = 1$ isotopes is shown in Fig. 3. The projection onto the $\Delta_{\rm TOF}$ axis is shown in Fig. 4. Also shown is the decomposition into particle type exploiting both the $\Delta_{\rm fast}$ and $\Delta_{\rm TOF}$ information. The p-d separation is quite good, but there is an overlap between the d and t isotopes.

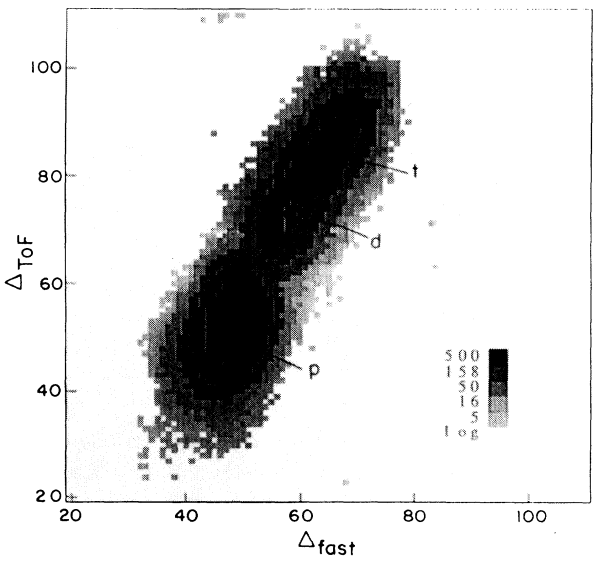

FIG. 3. $\Delta_{\rm fast}$ (x axis) vs $\Delta_{\rm TOF}$ (y axis) for $Z = 1$. $\Delta_{\rm fast}$ is the measured "fast" minus the "fast" expected from protons. $\Delta_{\rm TOF}$ is the measured time of flight (TOF) minus the TOF expected for protons.

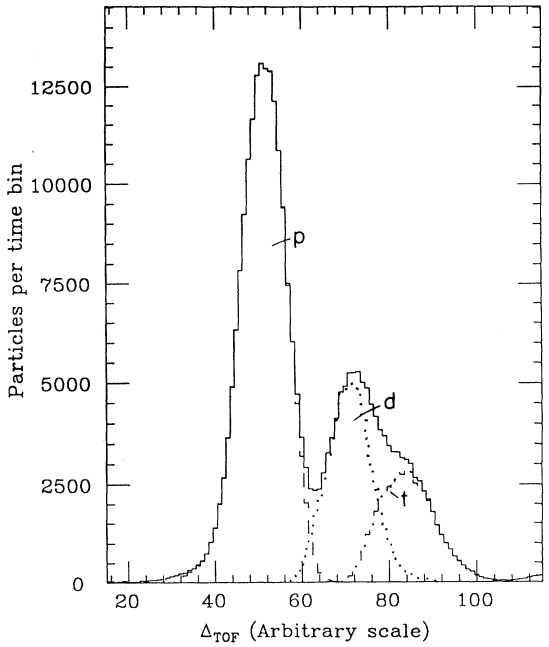

FIG. 4. Projection of Fig. 3 onto the $\Delta_{\rm TOF}$ axis. Also shown is the isotopic decomposition.

B. Evaporation residue detection

Evaporation residues were detected using a 20-μm-thick transmission-mounted silicon surface barrier detector. This was sufficiently thick to stop the residues, while the elastically scattered beam particles only deposited about 9 MeV. A 150-μm-thick veto detector was mounted behind the ER detector to veto elastic events. The detector was 4 in. from the target and was placed at either 12° or 16° for most of the measurements reported here. These angles were chosen to optimize the ER to elastic ratio. The residues are identified by their location on an energy versus time-of-flight (TOF) scatter plot, as illustrated in Fig. 5.

There is a kinematic correlation between the LCP's and ER's. To get enough information to correct for this we took data with the ER telescope at 12° and 16°, both opposite and on the same side of the beam as the phoswich array. Some of the phoswich detectors were partially shadowed when the ER telescope was on the same side and these were excluded in the analysis.

C. Fission fragment detection and cross-section results

Fission fragments were detected in a surface barrier detector usually located at 145° with respect to the beam. Some measurements were also made at 30°. Absolute differential cross sections were determined from the known target thickness, beam current, and geometrical efficiencies. The total fission cross sections were obtained by integrating over angle assuming the angular distribution measured by Vaz *et al.* [17]. Measuring at 145° minimizes

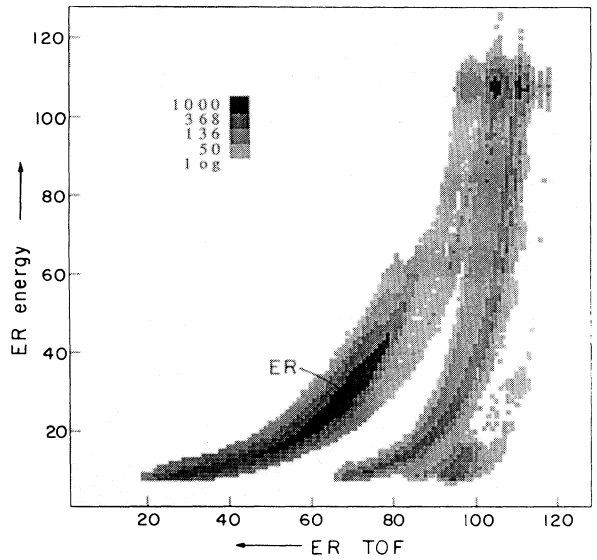

FIG. 5. Evaporation residue energy vs time of flight (TOF) scatter plot. The vertical axis is the measured pulse height. TOF increases from right to left along the horizontal axis.

the sensitivity to the fission fragment anisotropy. The fission cross sections obtained are tabulated in Table I. The fission cross section for Ta is in good agreement with the value of 1529±138 mb measured at 215 MeV by Vaz *et al.* Gavron *et al.* [18] report fission cross sections at 216 MeV for ^{142}Nd, ^{170}Er, and ^{192}Os which interpolate fairly well with our values in Table I. Their cross sections appear to be a little lower than ours, and for ^{238}U they report a value of 1845±185 to be compared with the value of 2375±214 reported by Vaz *et al.* We include results of measurements with an Ir target, although we did not measure LCP coincidences with this target due to the similarity with the Au target as far as the ℓ range of the tag is concerned.

III. FUSION CROSS SECTIONS AND MEAN ℓ FOR EVAPORATION RESIDUE AND FISSION TAGS

Absolute evaporation residue cross sections for these systems have not been measured in this work or reported in the literature. As we will want to deduce the mean ℓ for the ER and FF tags by making a sharp cutoff assumption, we need to have an estimate of the total fusion cross section in order to obtain the ER cross section by subtracting the fission cross section. We assume that the fusion cross section scales as

$$\sigma_{\text{fuse}} = \pi r_0^2 (A_1^{1/3} + A_2^{1/3})^2 (1 - B/E), \quad (1)$$

where the Coulomb barrier B is given by $Z_1 Z_2 e^2 / 1.44(A_1^{1/3}+A_2^{1/3})$. This relationship predicts only a 5% increase in the fusion cross section in going from Tb to Au so the required scaling is very modest. We can estimate the parameter r_0 in Eq. (1) in two ways. In the first method we assume that for Au there are no ER and that the fusion cross section equals the fission cross section (2030 mb). This is consistent with the fact that we did not observe many ER's for Au (we do not report LCP in coincidence with ER for Au because the tag rate was too low). The second method assumes that the fission cross section for ^{238}U is all associated with fusion, and that the fusion cross section for other targets scales as Eq. (1). This should be an upper limit, as peripheral nonfusion processes can also lead to fission for a very fissionable target like ^{238}U [19]. Scaling the average of the ^{238}U fission cross section of Vaz *et al.* [17] and of Gavron *et al.* [18] at 215 MeV leads to a Au fusion cross section 4% higher than our first estimate. We have chosen the first method which leads to an r_0 value in Eq. (1) of 1.21 fm. We list the deduced fusion and evaporation cross sections in Table I. We estimate that the fusion and hence the evaporation cross sections are uncertain by 200 mb. Also listed are the mean ℓ values for the ER and fission tags assuming a sharp cutoff in the ℓ ranges contributing to ER and to fission. We have used the ℓ values deduced from the 224-MeV-fission cross section in interpreting the 215-MeV-coincidence data as the evaporation-fission competition depends more strongly on ℓ than on excitation energy.

The ℓ boundary between evaporation residue and fission is of course not expected to be sharp. We have performed statistical model calculations with the code PACE [20] to assess the diffuseness in ℓ space of this competition. The result is compared with the sharp cutoff approximation in Fig. 1. The PACE calculations we have performed do not explicitly take into account the nuclear dissipation slowing down of the fission decay. A recent calculation [21] shows that incorporation of the nuclear dissipation effect leads to a negligible change of the mean angular momentum for the evaporation residue and fission fragment tags. We have also added a diffuseness

TABLE I. Fission cross section for 224 MeV ^{16}O on various targets. Also shown are the deduced fusion and evaporation residue (ER) cross sections (see text) and the mean ℓ values for the ER and fission tags. $\langle\ell\rangle$ is measured in $\hbar$ and $\langle b\rangle$ is measured in fm.

	σ_F (mb)	σ_{fusion} (mb)	σ_{ER} (mb)	$\langle\ell\rangle_{\text{ER}}$	$\langle b\rangle_{\text{ER}}$	$\langle\ell\rangle_{\text{FF}}$	$\langle b\rangle_{\text{FF}}$
^{159}Tb	500±30	1932	1432±200	54±4	5.5	87±5	8.8
^{181}Ta	1420±120	1974	554±200	34^{+6}_{-8}	3.5	77±6	7.9
$^{\text{nat}}$Ir	2020±160	1990	30^{+200}_{-30}	8^{+14}_{-8}	1.4	65±4	6.7
^{197}Au	2030±160	2030	0	0^{+14}_{-0}	1.4	65±4	6.7

to the fusionlike cross section as indicated by the dotted curve. The mean values for the ER and FF tags are not significantly different for the sharp and diffuse distributions and we have used the sharp cutoff values in presenting the results which follow.

One might wonder whether the difference in Coulomb barriers for the different systems significantly perturbs the ℓ values which would be expected to give the same preequilibrium particle emission. If one makes a simple estimate based on the assumption that the emission rate depends on the radial energy at contact, then the correction to ℓ for the Au target compared to that for the Tb target is less than 4%. This is as small as it is because of a fortuitous partial cancellation between the system dependence of the Coulomb barrier and the rotational energy arising from the μR^2 term in the denominator of the rotational energy.

IV. MOVING SOURCE PARAMETRIZATION OF LIGHT CHARGED PARTICLES

The total LCP multiplicity is defined as

$$M_{\mathrm{LCP}} = \frac{N_{\mathrm{LCP-tag}}}{N_{\mathrm{tag}}}, \tag{2}$$

where the tag is FF or ER, N_{tag} is the number of tags, and $N_{\mathrm{LCP-tag}}$ is the number of coincident events. Since we did not measure all LCP's or all tags, we must correct for detection efficiencies:

$$M_{\mathrm{LCP}} = \frac{N^{\mathrm{obs}}_{\mathrm{LCP-tag}}/\epsilon_{\mathrm{LCP-tag}}}{N^{\mathrm{obs}}_{\mathrm{tag}}/\epsilon_{\mathrm{tag}}}. \tag{3}$$

Here $N^{\mathrm{obs}}_{\mathrm{LCP-tag}}$ is the number of observed coincident events, and $\epsilon_{\mathrm{LCP-tag}}$ is the efficiency to detect LCP's in coincidence with tags. Likewise, $N^{\mathrm{obs}}_{\mathrm{tag}}$ is the number of observed tags, detected with an efficiency of ϵ_{tag}.

Ideally, the probability to detect the LCP would be independent of the probability to detect the tag, and we would have

$$\epsilon_{\mathrm{LCP-tag}} = \epsilon_{\mathrm{LCP}}\epsilon_{\mathrm{tag}} \tag{4}$$

and ϵ_{tag} would cancel out of Eq. (3). In the case of the ER tag the LCP detection *was* influenced by the detection of the tag. We discuss how we account for these correlations in Sec. V B and finish the discussion of the simpler FF tag here.

To extract the total number of LCP's it is necessary to integrate over the energy spectra and the angular distribution. This is most conveniently done by parametrizing the data by a moving source. We have chosen a parametrization based on isotropic volume emission [22], for which the energy spectrum in the moving frame is given by

$$\frac{d^2M}{d\Omega\, dE} = \frac{M}{2(\pi T)^{3/2}}(E - V_c)^{1/2}\exp\left[-(E - V_c)/T\right], \tag{5}$$

where M is the total multiplicity and T and V_c are the apparent source temperature and minimum Coulomb energy of the emitted particles. This parametrization assumes a Coulomb energy in the moving source frame following the work of Wada *et al.* [22] rather than a Coulomb energy in the laboratory frame assumed by Awes *et al.* [14]. If we fit our data with the Coulomb energy in the laboratory frame we find source velocities close to one-half the beam velocity, temperatures in the 4–5-MeV range, and Coulomb energies around 10 MeV for p, d, and t and 20 MeV for α. We have chosen to put the Coulomb barrier in the moving source frame because this makes the model more self-consistent. In this case we find source velocities approaching 70% of the beam velocity, temperatures in the 7–8-MeV range and Coulomb energies around 2 MeV for p, d, and t and 5 MeV for α. Both parametrizations give reasonable χ^2 values for the best fits.

The spectra are transformed to the laboratory system using

$$\left[\frac{d^2M}{d\Omega\, dE}\right]_{\mathrm{lab}} = \left[\frac{E_{\mathrm{lab}}}{E'}\right]^{1/2}\left[\frac{d^2M}{d\Omega\, dE}\right]_{E=E'} \tag{6}$$

where $E' = E_{\mathrm{lab}} - 2(\frac{1}{2}m_{\mathrm{LCP}}v_s^2E_{\mathrm{lab}})^{1/2}\cos(\theta) + \frac{1}{2}m_{\mathrm{LCP}}v_s^2$ and v_s is the moving source velocity. There is no fundamental reason for preequilibrium particle emission to have the assumed functional form of Eq. (5) or to originate from a single moving source velocity. We have, however, found that such a parametrization provides an adequate representation of preequilibrium proton emission as calculated by a realistic nucleon exchange transport [12] model. A fit to that part of the calculated proton spectrum within our angular range for 224 MeV ^{16}O + ^{181}Ta yielded a fit with $\chi^2_\nu = 3.2$, an apparent temperature of 5.5 MeV, and a source velocity to projectile velocity ratio of 0.4. Since our interest in this study is the variation of multiplicity with impact parameter, we are primarily interested in variations of the multiplicity depending on the tag. A moving source fit which adequately reproduces the data should provide a quantitative determination of any dependence of multiplicity on impact parameter.

In addition to the moving source characterizing the preequilibrium emission, we have added a second source of the form

$$\frac{d^2M_{\mathrm{equil}}}{d\Omega\, dE} = \frac{M_{\mathrm{equil}}}{4\pi T^2_{\mathrm{equil}}}(E - V_{\mathrm{equil}}) \times \exp\left[-(E - V_{\mathrm{equil}})/T_{\mathrm{equil}}\right] \tag{7}$$

to account for surface evaporation from the composite system moving at the center of mass velocity. This source is only important at the more backward angles and lower LCP energies. Since our data are dominated by preequilibrium particles, we do not expect our fits to constrain the equilibrium source very well. We fix the temperature of the equilibrium source at $T_{\mathrm{equil}} = 2.75$ MeV which is typical of the excitation energies for these reactions. Similarly, we fix the Coulomb barrier of the equilibrium source at its expected value of $V_{\mathrm{equil}} = 8.6$ MeV for p, d, t, and 17.2 MeV for α. We allow the remaining parameter, M_{equil}, to be set by the fit.

In order to avoid any problems associated with variations of detection efficiency with energy close to the par-

ticle identification threshold and to minimize the effect of the evaporation source, we have restricted our fits to laboratory energies well above the threshold. For protons the minimum energies considered were 12.5 and 17.5 MeV for detectors without and with Ta cover foils.

We estimate the moving source parameters by minimizing

$$\chi^2 = \sum_i \sum_E \frac{[C(E,i) - N(E,i)]^2}{C(E,i)}. \quad (8)$$

The statistical uncertainty is dominated by $N(E,i)$, the number of detected LCP in energy bin E and phoswich counter i. $C(E,i)$ is the expected number of counts with energy E in phoswich counter i, and is calculated as

$$C(E,i) = \frac{\epsilon_{\text{LCP-tag}}}{\epsilon_{\text{tag}}} N_{\text{tag}} \frac{d^2M}{d\Omega\, dE}. \quad (9)$$

We use the expected number of counts as the weight (as opposed to the observed number of counts) since some of the bins have very few counts.

The χ^2 minimization was done with an iterative fit routine. This procedure has been checked by fitting Monte Carlo generated data. The Monte Carlo event generation, which was necessary for the ER data analysis, is described in Appendix B.

V. RESULTS OF FITS TO MOVING SOURCE

A. Moving source fits to FF-tagged data

When examining data tagged by fission fragments one must consider the possibility of an azimuthal dependence of the LCP relative to the plane defined by the beam and the detected fission fragment. Such correlations have been studied by several groups [23–26], and the trends can be summarized as follows. The azimuthal anisotropy increases with increasing mass of the LCP. For a given kind of LCP, the anisotropy increases with both LCP kinetic energy and angle. We only measured the azimuthal dependence at small polar angles. The proton azimuthal dependence is consistent with isotropy, while the alphas show some anisotropy. Our results for deuterons and tritons had too poor statistics to define an azimuthal dependence. Guided by previous work and our own results, we have parametrized the ϕ dependence of the LCP by the functional relationship

$$W(\phi) = 1 + amE \sin\theta \cos^2\phi, \quad (10)$$

where θ is the angle from the beam, ϕ is measured from the plane of the detected FF, and m and E are the mass and laboratory energy of the LCP. A value of 0.005 for the parameter a was found to reproduce the average trend exhibited by the data for the three targets. This value typically leads to a decrease of about 20% for the alpha particle multiplicity compared to the value obtained neglecting the azimuthal dependence. The effect on the multiplicities of the other particles is smaller than this. To determine the moving source parameters we use Eq. (8) by modifying Eq. (9) to read

$$C(E,i) = \epsilon_{\text{LCP}} W(\phi) N_{\text{FF}} \frac{d^2M}{d\Omega\, dE}. \quad (11)$$

We have taken fission fragment tagged data with Tb, Ta, and Au targets. The moving source parameters for the FF tagged data are listed in Table II. The error

TABLE II. Moving source fits for fission fragment tagged data. The temperature and Coulomb barrier of the equilibrium source have been fixed, but there is no constraint on the moving source.

Tgt	χ^2_ν	M	v_s/v_{beam}	T	V_c	M_{equil}
			Protons			
Tb	0.88	0.131 ± 0.019	0.71 ± 0.05	7.1 ± 0.5	1.3 ± 0.7	0.13 ± 0.02
Ta	1.23	0.189 ± 0.010	0.60 ± 0.02	7.8 ± 0.2	2.3 ± 0.2	0.10 ± 0.01
Au	1.26	0.215 ± 0.007	0.66 ± 0.02	7.1 ± 0.1	2.5 ± 0.1	0.10 ± 0.01
Avg	–	0.178 ± 0.005	0.66 ± 0.01	7.33 ± 0.10	$2.0 \pm .1$	0.097 ± 0.006
			Deuterons			
Tb	1.03	0.053 ± 0.008	0.66 ± 0.09	6.8 ± 0.6	1.4 ± 0.7	0.017 ± 0.010
Ta	1.02	0.061 ± 0.003	0.64 ± 0.03	7.8 ± 0.3	1.6 ± 0.2	0.018 ± 0.004
Au	1.30	0.074 ± 0.003	0.64 ± 0.03	7.4 ± 0.2	1.5 ± 0.1	0.014 ± 0.004
Avg	–	0.063 ± 0.002	0.65 ± 0.02	7.3 ± 0.15	$1.5 \pm .1$	0.013 ± 0.003
			Tritons			
Tb	1.06	0.034 ± 0.004	0.74 ± 0.10	7.7 ± 0.6	0.2 ± 0.5	0.006 ± 0.007
Ta	1.21	0.039 ± 0.002	0.73 ± 0.04	8.1 ± 0.3	0.3 ± 0.2	0.009 ± 0.003
Au	1.02	0.047 ± 0.002	0.69 ± 0.03	7.3 ± 0.2	0.8 ± 0.2	0.007 ± 0.003
Avg	–	0.040 ± 0.001	0.72 ± 0.02	7.70 ± 0.15	$0.43 \pm .12$	0.007 ± 0.002
			Alphas			
Tb	0.95	0.181 ± 0.012	0.67 ± 0.05	6.4 ± 0.2	3.9 ± 0.3	0.12 ± 0.16
Ta	1.47	0.217 ± 0.004	0.68 ± 0.02	6.8 ± 0.1	4.5 ± 0.1	0.42 ± 0.06
Au	2.12	0.298 ± 0.005	0.70 ± 0.01	6.4 ± 0.1	4.7 ± 0.1	0.95 ± 0.06
Avg	–	0.232 ± 0.003	0.68 ± 0.01	6.53 ± 0.04	$4.4 \pm .01$	0.50 ± 0.04

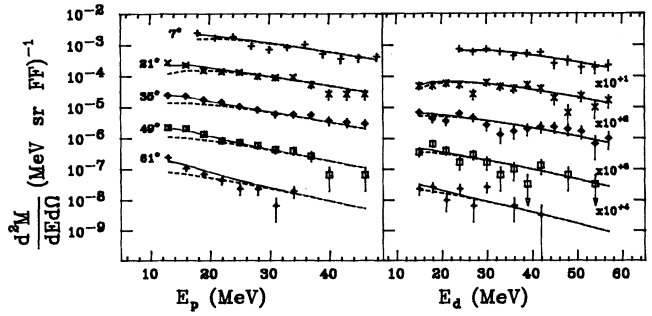

FIG. 6. $\frac{d^2M}{d\Omega\, dE}$ vs E for protons and deuterons in coincidence with fission fragments. Points with error bars are the data for the Ta target. Dashed lines are the moving source fits to the data while the solid lines are the sum of the moving and equilibrium sources. Only data for counters at 7°, 21°, 35°, 49°, and 61° are shown for clarity.

bars are statistical only. We assign a 10% systematic uncertainty to the FF tagged multiplicities to reflect possible errors in the use of $W(\phi)$. The multiplicities are integrated over all energies, not just above the detection threshold. Typical fits are shown in Figs. 6 and 7. For clarity, only a few of the phoswich counters are included.

The fit values of the Coulomb barriers have a reasonable trend, for a given Z the higher A values have a lower V_c, and as Z increases so does V_c. The actual values seem low, but one must remember that the functional form chosen for convenience to parametrize the LCP's has no fundamental justification and the parameters other than the source velocity and multiplicity do not have a direct physical interpretation. The apparent temperatures are independent of the target, although d and t have a higher temperature than p and α.

The source velocity is about 65% of the beam velocity and is independent of the target and the light particle.

The multiplicities of the equilibrium source are small with the exception of the α data. Even for the α data the equilibrium source is very small compared to the preequilibrium source over the range of angles and energies measured in this experiment.

We are primarily interested in the multiplicities of the prompt particles. As the average impact parameter decreases the prompt particle multiplicity increases.

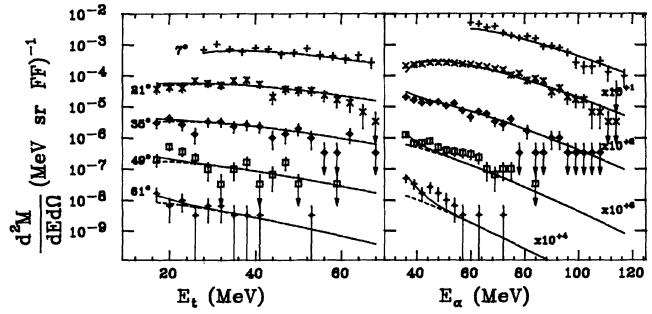

FIG. 7. $\frac{d^2M}{d\Omega\, dE}$ vs E for tritons and alphas in coincidence with fission fragments. Points with error bars are the data for the Ta target. Dashed lines are the moving source fits to the data while the solid lines are the sum of the moving and equilibrium sources. Only data for counters at 7°, 21°, 35°, 49°, and 61° are shown for clarity.

B. Moving source fits to evaporation residue-tagged data

We also have taken ER tagged data with the same targets. We divide each of these sets in two, one with the ER telescope at ±12° and one with the ER telescope at ±16°. We would have a total of six data sets but the evaporation residue cross section for Au data is too small to give meaningful statistics.

In the ER analysis we must take account of the compound nucleus recoil from the LCP. The ER yield falls off very rapidly with angle as the detector is moved away from 0°. An LCP emitted at a nonzero angle can kick the recoil either toward or away from the ER detector, leading to a bias in the ER detection efficiency for coincident events relative to the ER singles events. This effect is strongest for α particles because of their larger mass and higher kinetic energy. A 75-MeV α measured at 50° will be momentum balanced by an ER at 16° on the opposite side of the beam whereas a 50-MeV proton measured at 50° will only kick the ER to 5.7°. This correlation between the LCP emission energy and angle and the ER detection efficiency must be accounted for.

Formally we use Eq. (8) as the definition of χ^2 by modifying Eq. (9) to read

$$C(E,i) = \epsilon_{\mathrm{LCP-ER}}(E,i)\frac{N_{\mathrm{ER}}}{\epsilon_{\mathrm{ER}}}\frac{d^2M}{d\Omega\, dE}, \tag{12}$$

where E is the energy of the LCP and i is the phoswich counter index. Here we explicitly recognize $\epsilon_{\mathrm{LCP-ER}}(E,i)$ depends on the energy and type of LCP detected. We must calculate the coincidence efficiency as a function of LCP energy for each type of LCP and each phoswich counter. Implicit is the recognition that $\epsilon_{\mathrm{LCP-ER}}(E,i)$ and ϵ_{ER} depend on the LCP's that are emitted but not detected.

We calculate $\epsilon_{\mathrm{LCP-ER}}(E,i)$ and ϵ_{ER} using Monte Carlo techniques. For $\epsilon_{\mathrm{LCP-ER}}(E,i)$, we loop over the phoswich counter, then over the LCP type, then over the energy of the LCP. We generate a random direction for the LCP within the counter, then calculate the recoil direction and momentum of the ER. (We assume full momentum transfer from the beam to the compound nucleus.) We smear the ER direction and energy to account for particle evaporation from the equilibrated compound nucleus, then modify the ER direction and energy to account for multiple Coulomb scattering and dE/dx in the target. If the ER would enter the ER detector with an energy above the detection threshold we "detect" the event. The coincident efficiency, $\epsilon_{\mathrm{LCP-ER}}(E,i)$, is the ratio of "detected" events to generated events.

The calculation of ϵ_{ER} is very similar. For each event we generate a group of LCP's distributed randomly ac-

TABLE III. Moving source fits for evaporation residue tagged data. The temperature and Coulomb barrier of the equilibrium source have been fixed, but there is no constraint on the moving source.

Tgt	Angle	χ^2_ν	M	v_s/v_{beam}	T	V_c	M_{equil}
			Protons				
Tb	12°	2.8	0.227 ± 0.008	0.74 ± 0.01	6.2 ± 0.1	0.9 ± 0.2	0.33 ± 0.01
Tb	16°	3.5	0.209 ± 0.005	0.77 ± 0.01	6.1 ± 0.1	1.1 ± 0.1	0.38 ± 0.01
Ta	12°	3.1	0.286 ± 0.007	0.77 ± 0.01	5.8 ± 0.1	1.5 ± 0.1	0.21 ± 0.01
Ta	16°	2.6	0.275 ± 0.007	0.78 ± 0.01	5.5 ± 0.1	1.5 ± 0.1	0.228 ± 0.012
Avg	–	–	0.244 ± 0.003	0.77 ± 0.01	5.82 ± 0.04	$1.41 \pm .05$	0.297 ± 0.006
			Deuterons				
Tb	12°	2.1	0.075 ± 0.002	0.66 ± 0.01	6.5 ± 0.1	1.6 ± 0.1	0.054 ± 0.005
Tb	16°	3.0	0.068 ± 0.001	0.65 ± 0.01	6.6 ± 0.1	1.5 ± 0.1	0.071 ± 0.004
Ta	12°	2.3	0.092 ± 0.003	0.67 ± 0.01	6.4 ± 0.1	1.3 ± 0.2	0.049 ± 0.005
Ta	16°	2.3	0.088 ± 0.002	0.65 ± 0.01	6.0 ± 0.1	1.6 ± 0.1	0.048 ± 0.006
Avg	–	–	0.077 ± 0.001	0.65 ± 0.01	6.35 ± 0.05	$1.56 \pm .06$	0.058 ± 0.003
			Tritons				
Tb	12°	1.9	0.030 ± 0.001	0.69 ± 0.01	6.7 ± 0.2	0.6 ± 0.3	0.021 ± 0.003
Tb	16°	3.0	0.037 ± 0.001	0.67 ± 0.01	6.9 ± 0.1	0.7 ± 0.1	0.037 ± 0.003
Ta	12°	2.5	0.038 ± 0.001	0.62 ± 0.01	7.0 ± 0.2	1.1 ± 0.3	0.009 ± 0.003
Ta	16°	2.5	0.043 ± 0.001	0.68 ± 0.01	6.2 ± 0.1	0.7 ± 0.2	0.031 ± 0.005
Avg	–	–	0.037 ± 0.005	0.67 ± 0.01	6.63 ± 0.06	$0.72 \pm .10$	0.021 ± 0.002
			Alphas				
Tb	12°	5.3	0.188 ± 0.012	0.76 ± 0.01	7.1 ± 0.1	0.0 ± 0.7	1.08 ± 0.05
Tb	16°	9.3	0.147 ± 0.002	0.70 ± 0.01	6.4 ± 0.1	4.0 ± 0.1	1.40 ± 0.05
Ta	12°	6.3	0.186 ± 0.006	0.71 ± 0.01	7.2 ± 0.1	1.8 ± 0.4	0.85 ± 0.05
Ta	16°	7.2	0.175 ± 0.002	0.67 ± 0.01	6.3 ± 0.1	4.3 ± 0.1	1.43 ± 0.08
Avg	–	–	0.160 ± 0.001	0.70 ± 0.01	6.46 ± 0.02	$4.11 \pm .06$	1.15 ± 0.03

cording to a set of moving source parameters. The recoil of the ER is calculated, the ER energy and direction are smeared to account for equilibrium evaporation and passage through the target. Finally ER's heading into the ER detector above threshold are detected. ϵ_{ER} is the ratio of detected ER's to generated events. The Monte Carlo calculations are described in more detail in Appendix B.

The moving source parameters for the ER tagged data are listed in Table III. The error bars are statistical only. We assign a 15% systematic uncertainty to the ER tagged multiplicities to reflect possible errors in the calculation of $\epsilon_{\text{LCP-ER}}(E, i)$. Typical fits are shown in Figs. 8–11. In these figures the data have been efficiency corrected. For clarity, only a few of the phoswich counters are included.

The ER tagged fits have a larger χ^2 than the FF tagged fits. The source velocity is slightly higher and the tem-

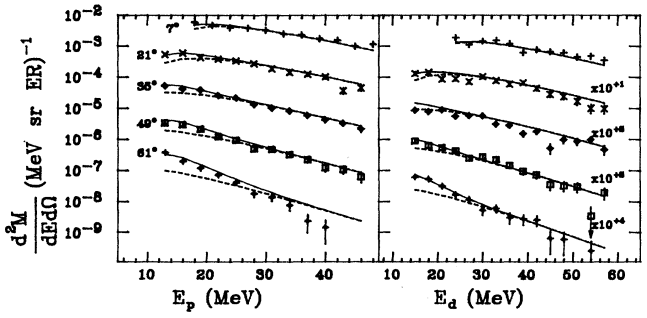

FIG. 8. $\frac{d^2M}{d\Omega\, dE}$ vs E for protons and deuterons in coincidence with evaporation residues. Here the Ta data are presented with the evaporation residue counter located at 16°. Points with error bars are the data after correction for coincidence efficiency. Dashed lines are the moving source fits to the data while the solid lines are the sum of the moving and equilibrium sources. Only data for counters at 7°, 21°, 35°, 49°, and 61° are shown for clarity.

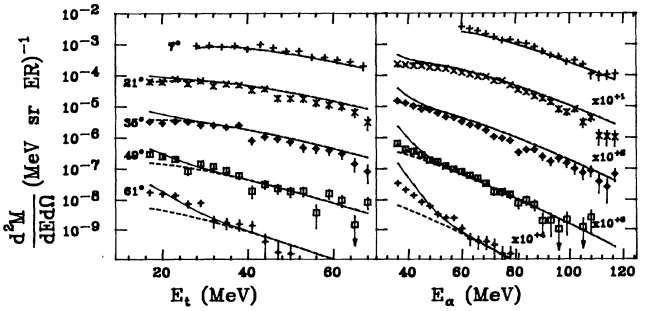

FIG. 9. $\frac{d^2M}{d\Omega\, dE}$ vs E for tritons and alphas in coincidence with evaporation residues. This is the Ta data with the evaporation residue counter located at 16°. Points with error bars are the data after correction for coincidence efficiency. Dashed lines are the moving source fits to the data while the solid lines are the sum of the moving and equilibrium sources. Only data for counters at 7°, 21°, 35°, 49°, and 61° are shown for clarity.

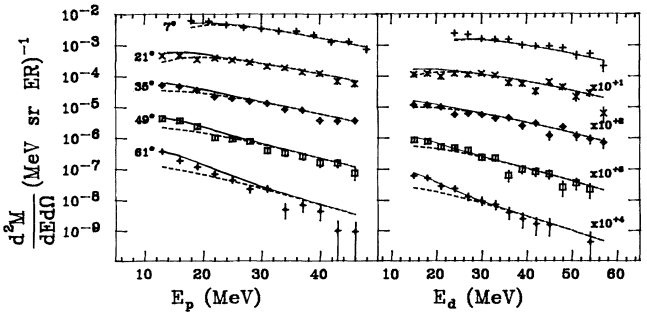

FIG. 10. $\frac{d^2M}{d\Omega\, dE}$ vs E for protons and deuterons in coincidence with evaporation residues. This is the Ta data with the evaporation residue counter located at 12°. Points with error bars are the data after correction for coincidence efficiency. Dashed lines are the moving source fits to the data while the solid lines are the sum of the moving and equilibrium sources. Only data for counters at 7°, 21°, 35°, 49°, and 61° are shown for clarity.

perature and Coulomb barriers are slightly lower for the ER tagged fits compared to the FF tagged fits. The agreement between the 12° and 16° data is reasonably good, particularly for protons and deuterons.

C. Comparison of fission fragment and evaporation residue multiplicities

A moving source parametrization of our FF and ER tagged data describes our LCP data fairly well. We used five parameters; the prompt light particle multiplicity, moving source velocity, source temperature, Coulomb barrier, and equilibrium light particle multiplicity. The source velocity, temperature, and Coulomb barrier are independent of target although there does seem to be a difference between the two tag types. It is not clear whether this is due to an inadequacy in the recoil corrections for the ER tag or to a real effect. Since we are interested in the LCP multiplicity dependence on the impact parameter, we fix the source velocity, temperature, and Coulomb barriers at their average values and refit for multiplicities. These average values are $v_s/v_{\rm beam} = 0.679$, $T = 6.46$ MeV, $V_c(p) = 2.40$ MeV, $V_c(d) = 1.57$ MeV, $V_c(t) = 0.89$ MeV, and $V_c(\alpha) = 4.69$ MeV. These multiplicities are listed in Table IV. The multiplicities obtained with the compromise set of parameters generally differ by less than 10% from the values in Tables II and III.

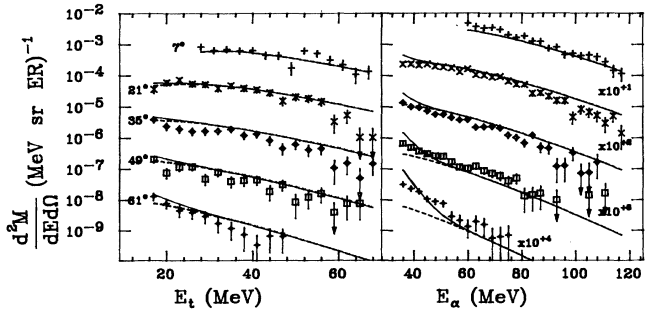

FIG. 11. $\frac{d^2M}{d\Omega\, dE}$ vs E for tritons and alphas in coincidence with evaporation residues. Here the Ta data are presented with the evaporation residue counter located at 12°. Points with error bars are the data after correction for coincidence efficiency. Dashed lines are the moving source fits to the data while the solid lines are the sum of the moving and equilibrium sources. Only data for counters at 7°, 21°, 35°, 49°, and 61° are shown for clarity.

We display these multiplicities graphically by plotting them as a function of mean angular momentum (proportional to impact parameter) in Fig. 12. The mean angular momenta are taken from Table I. The horizontal error bars in Fig. 12 reflect the uncertainty in the mean ℓ values, not the width of the ℓ distribution sampled. The vertical error bars represent possible systematic errors in the multiplicity determination and are 10% for the FF tagged data and 15% for the ER tagged data.

One noticeable feature of Fig. 12 is that the p, d, and t multiplicities vary nearly monotonically with the mean angular momentum, while the alpha multiplicities have a significant step at the change in tag type. We have considered a number of possible causes of the latter step. One might be inadequacies in the calculation of the recoil effect correction for the ER tagged data. We have some reassurance that this is not likely a major effect because the 12° and 16° ER detector angle multiplicities agree. The recoil corrections differ appreciably between 12° and 16°. A second possibility is that there are alphas accompanying or following fission not present when evaporation residues are formed. In fact alphas are emitted during scission but with such a low probability (1 in 300) and with such low average energies that their contribution would be negligible. Postfission evaporation alphas would also be of fairly low energy and enhanced in the direction of the fragment complementary to the backward-detected fission fragment. Such an enhancement is not observed. A third possibility, and one which we think more likely, is associated with an increasing contribution of peripheral processes with increasing target fissility. This idea is explained further in the next section.

VI. DISCUSSION

A. Dependence of complex-particle to proton multiplicity ratio on impact parameter

The differing behavior of the complex particle as compared to proton multiplicities can be exhibited more clearly by plotting the ratio of the d, t, and alpha multiplicities to the proton multiplicities. These ratios are shown in Fig. 13. The d/p and t/p ratios increase monotonically with impact parameter. This rules out any mechanism which does not depend on the dynamics of the reaction, such as surface emission or the simple coalescence model. The qualitative behavior of the α/p ratio continues the trend observed by Awes *et al.* for more peripheral processes, where they saw a higher α/p ratio for very peripheral events with small momentum transfer.

TABLE IV. Moving source fits to LCP data. We have fixed $v_s/v_{\rm beam} = 0.679$, $T = 6.46$ MeV, $V_c(p) = 2.40$ MeV, $V_c(p) = 1.57$ MeV, $V_c(p) = 0.89$ MeV, and $V_c(\alpha) = 4.69$ MeV. The errors listed are statistical. We estimate the systematic errors to be 10% for the FF tagged data and 15% for the ER tagged data.

Tgt	$\langle\ell\rangle$	χ^2_ν	M	$M_{\rm equil}$
	Protons			
Tb FF	87 ± 5	0.90	0.138 ± 0.006	0.123 ± 0.013
Ta FF	77 ± 6	1.60	0.153 ± 0.003	0.119 ± 0.005
Au FF	65 ± 4	1.44	0.203 ± 0.003	0.103 ± 0.005
Tb ER	54 ± 4	4.7	0.228 ± 0.002	0.405 ± 0.005
Ta ER	34^{+6}_{-8}	4.4	0.322 ± 0.003	0.260 ± 0.007
	Deuterons			
Tb FF	87 ± 5	1.02	0.059 ± 0.003	0.004 ± 0.007
Ta FF	77 ± 6	1.30	0.053 ± 0.001	0.019 ± 0.003
Au FF	65 ± 4	1.50	0.065 ± 0.001	0.019 ± 0.003
Tb ER	54 ± 4	2.5	0.065 ± 0.001	0.073 ± 0.003
Ta ER	34^{+6}_{-8}	2.34	0.085 ± 0.001	0.062 ± 0.004
	Tritons			
Tb FF	87 ± 5	1.11	0.039 ± 0.002	0.000 ± 0.006
Ta FF	77 ± 6	1.55	0.042 ± 0.001	0.004 ± 0.003
Au FF	65 ± 4	1.20	0.045 ± 0.001	0.007 ± 0.003
Tb ER	54 ± 4	2.5	0.035 ± 0.001	0.027 ± 0.002
Ta ER	34^{+6}_{-8}	2.6	0.038 ± 0.001	0.025 ± 0.003
	Alphas			
Tb FF	87 ± 5	0.94	0.144 ± 0.004	0.42 ± 0.11
Ta FF	77 ± 6	1.60	0.220 ± 0.002	0.49 ± 0.04
Au FF	65 ± 4	1.7	0.322 ± 0.002	0.73 ± 0.05
Tb ER	54 ± 4	8.3	0.155 ± 0.001	1.30 ± 0.03
Ta ER	34^{+6}_{-8}	7.5	0.167 ± 0.001	1.36 ± 0.04

B. Comparison with other experiments

In this section we compare our tagged multiplicities with results of measurements in which there has been some discrimination against peripheral events. Since these other measurements only distinguished fusionlike events from peripheral events, we have constructed multiplicities for fusionlike events by taking a weighted average of the ER- and FF-tagged multiplicities for each of the three targets. These fusionlike multiplicities are given in Table V. It is interesting to note that these fusionlike proton multiplicities are identical to within 5%, supporting the assumption that the change in multiplicity with target Z and A is small. We compare our proton multiplicities with those of Refs. [14, 22, 27, 28] in Fig. 14. We have chosen to plot these multiplicities versus (bombarding energy)/nucleon, as there is insufficient information available to establish a more sophisticated scaling. It appears, however, that our results are consistent with such a simple scaling. Rather than plotting the absolute d, t, and α multiplicities in the same way, we have chosen to plot the ratio of these multiplicities to the proton multiplicities, as shown in Fig. 15. Although there is considerably more scatter, it appears that the *ratio* of the complex particle to proton multiplicity does not vary much with bombarding energy. These ratios are observed to be several times lower for the very light Ne + Al system compared to the heavier systems. Our multiplicity ratios for deuterons and tritons are similar for our three targets, whereas the alpha-to-proton mul-

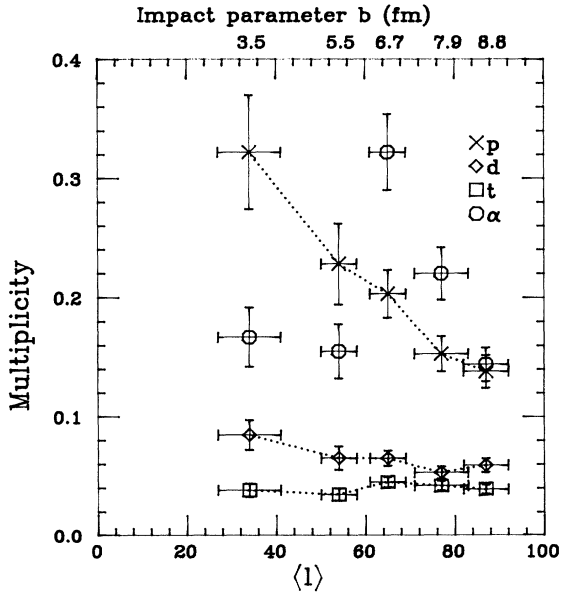

FIG. 12. Prompt particle multiplicities as a function of mean angular momentum. The horizontal error bars show the uncertainty in the mean ℓ values, not the width of the ℓ distribution sampled. The vertical error bars are the systematic errors. For the FF tagged data we use a 10% systematic error. For the ER tagged data we use a 15% systematic error to reflect possible problems in the calculation of $\epsilon_{\rm ER-LCP}$. The multiplicities for the same target but different ER runs agree to much better than 15%.

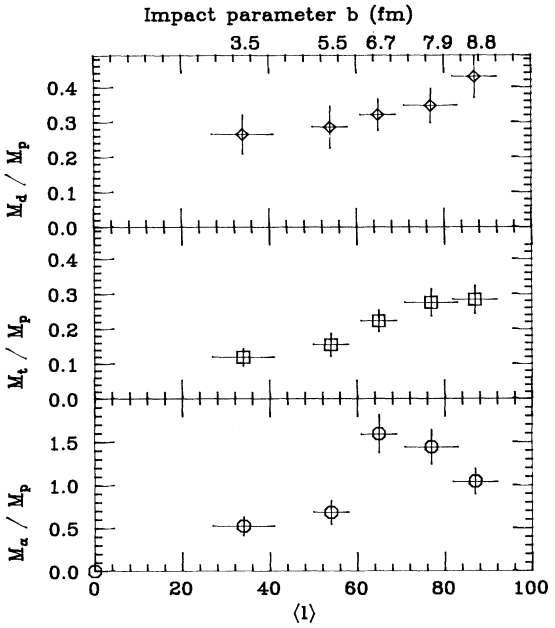

FIG. 13. Ratio of deuteron (top), triton (middle), and alpha (bottom) multiplicities to proton multiplicities as a function of mean angular momentum.

tiplicity ratio exhibits a surprisingly large variation with target. This variation arises primarily from the alpha multiplicity determined from the fission tag.

A possible explanation for the strong target dependence of M_α is that with increasing target fissility there is an increasing contribution of peripheral processes. The more fissile target nuclei can fission when a smaller fraction of the projectile is captured (such processes are sometimes characterized as breakup-fusion or massive transfer). This interpretation is supported by the results and interpretation of Wada *et al.* [22] who have measured p, d, t, and α yields in coincidence with evaporation residues for 30 MeV/nucleon ^{16}O and ^{32}S on Ag. They find that the p, d, and t multiplicities do not vary significantly with evaporation residue velocity, whereas the alpha multiplicity increases with decreasing residue velocity. They interpret this as indicating that alpha particles result primarily from the more peripheral collisions. Leegte *et al.* [29] come to a somewhat similar conclusion on the basis of rather different arguments. They compare angle-integrated spectra with coalescence model spectra generated from a Boltzmann master equation approach

TABLE V. Fusionlike multiplicities derived by weighted average of evaporation residue and fission tagged multiplicities.

Target	M_p	M_d	M_t	M_α
^{159}Tb	0.203	0.062	0.037	0.156
^{181}Ta	0.195	0.063	0.042	0.218
^{197}Au	0.195	0.066	0.047	0.345

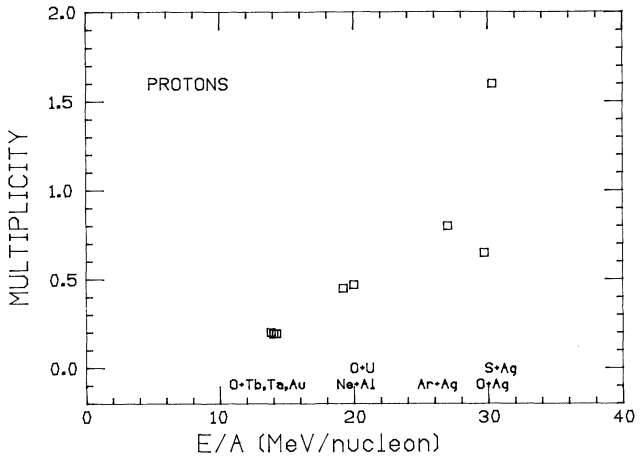

FIG. 14. Comparison of preequilibrium proton multiplicities for fusionlike collisions. The O + Tb, Ta, Au values are from this work, the Ne + Al, O + U, and Ar + Ag are from Refs. [14, 27, 28].

and attribute the excess of high energy particles to massive transfer reactions. For 30 MeV/nucleon ^{14}N + ^{232}Th they deduce about half of the preequilibrium tritons and alphas, and at least 1/3 of the deuterons are associated with more peripheral massive transfer processes. Our data do not show as near as large an effect for tritons although there is a hint of a discontinuity in our triton and deuteron multiplicities at the same place as for alphas, although diminished in magnitude.

The decrease in complex particle to proton multiplicity with decreasing impact parameter observed in our work as illustrated in Fig. 13 is opposite to the trend claimed by Peter *et al.* [16] in the ^{40}Ar + ^{27}Al reaction at 45 MeV/nucleon. It is not clear whether this difference results from the lighter system and higher energy in the latter work, or whether it is an artifact of the con-

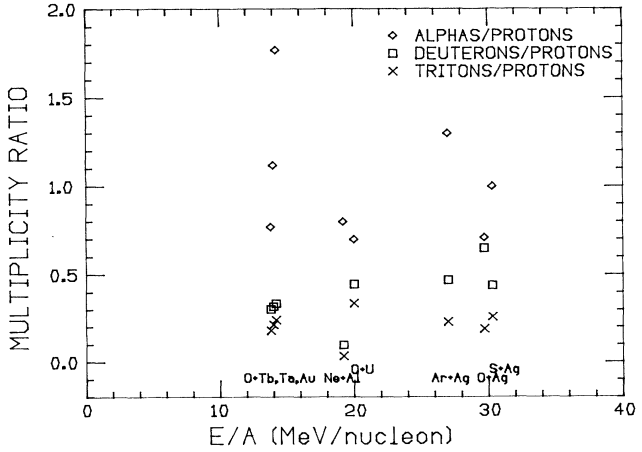

FIG. 15. Ratios of complex particle multiplicities to proton multiplicities for fusionlike collisions. The data are taken from the references given in the caption to Fig. 14.

struction of the impact parameter scale from the average parallel velocity. Detection of a preequilibrium alpha (as compared to a proton) in the backward direction in this reverse kinematics experiment (corresponding to forward direction in a normal kinematics experiment) will bias the parallel velocity in a way to make the collision appear more central.

The dependence of the proton multiplicity on the impact parameter that we have observed is in agreement with the dependence of the neutron multiplicity on the impact parameter observed in the ^{20}Ne + ^{165}Ho reaction by Holub *et al.* [2] at a similar E/A of 14.6 MeV/nucleon. They find a preequilibrium neutron multiplicity of 1.5 in coincidence with evaporation residues, and a multiplicity of 1.0 in coincidence with fission fragments. We estimate that these correspond to mean angular momenta of 40 and 60, respectively.

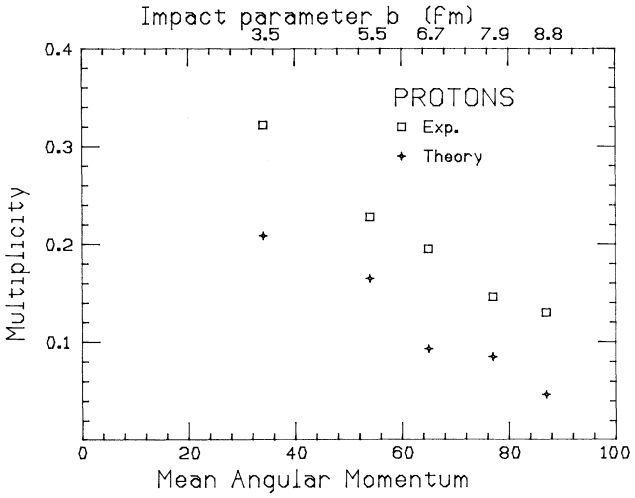

FIG. 16. Comparison of the dependence of experimental and theoretical proton multiplicities on mean angular momentum. The calculations have been performed for the relevant projectile-target combinations.

C. Comparison of proton multiplicities with nucleon exchange transport model

Preequilibrium protons emitted in the forward direction are generally attributed to protons from the projectile which escape at early stages in the fusion of the projectile and target. Models which take into account the coupling of the relative motion of the projectile-target system to the Fermi motion of the nucleons within the nuclei are often referred to as Fermi jet models. We have used a modified version [30] of such a model [12] to calculate the preequilibrium proton multiplicity for the different target and impact parameter bins. The modification consists of replacing the ground-state Fermi momentum distribution with a diffuse momentum distribution. The calculated results for projectile jetting are compared with the experimental proton multiplicities in Fig. 16. (Jets originating in the target would appear in the backward direction and not be observed in this study.) The model provides an excellent reproduction of the impact parameter dependence of the multiplicity, and a reasonable reproduction of the absolute magnitude considering that it is an *a priori* model without adjustable parameters. A comparison of the calculated and experimental energy spectra at different angles is presented elsewhere [31].

D. Coalescence model comparison

In the absence of a more fundamental model for complex particle formation, we compare our spectra for d, t, and alpha particles with a coalescence model. Such an analysis is often performed [14, 1, 33, 34] to describe the preequilibrium composite particle spectra starting from the corresponding proton spectra. The basic idea is that neutrons and protons can coalesce if they have similar average momenta. Neglecting Coulomb effects, the differential multiplicity of a complex particle with A nucleons

$$\frac{d^2M_A(E_A)}{dE_A d\Omega} = \text{const} \times \left[\frac{d^2M_p(E_p)}{dE_p d\Omega}\right]^A , \tag{13}$$

where $E_A = AE_p$. Thus the yield of a complex particle depends on the proton yield for particles with the same velocity. The proportionality constant depends on the coalescence radius in momentum space, p_0. This characterizes the allowable range in relative momenta the two particles can have and still be assumed to coalesce. The only predictive power of the model is the shape of the complex particle energy spectrum, with the normalization giving the coalescence radius.

This model is mainly based on phase-space arguments and does not include the dynamics of formation of the complex particles. This model is fairly successful in many cases where it has been found that the values of the temperature parameter T for p, d, t, α determined from a moving source model analysis of the respective energy spectra are nearly the same. In extending the coalescence model originally successfully applied at relativistic energies to nonrelativistic energies, suitable modification has been made [14, 1] to take into account the effect of the Coulomb repulsion of the charged particles from the target residue.

According to the modified coalescence model the differential multiplicity of the complex particles $d^2M[Z,N,E_A]/dE_A d\Omega$ consisting of Z protons and N neutrons ($A = Z + N$) with energy E_A is related to that of the proton $d^2M_p(E_p)/dE\, d\Omega$ as

$$\frac{d^2M[Z,N,E_A]}{dE_A d\Omega} = \left[\frac{N_t + N_p}{Z_t + Z_p}\right]^N \frac{A^{-1}}{N!Z!} \left[\frac{\frac{4}{3}\pi p_0^3}{[2m_0^3(E - E_C)]^{1/2}}\right]^{A-1} \left[\frac{d^2M_p(E_p)}{dE\, d\Omega}\right]^A . \tag{14}$$

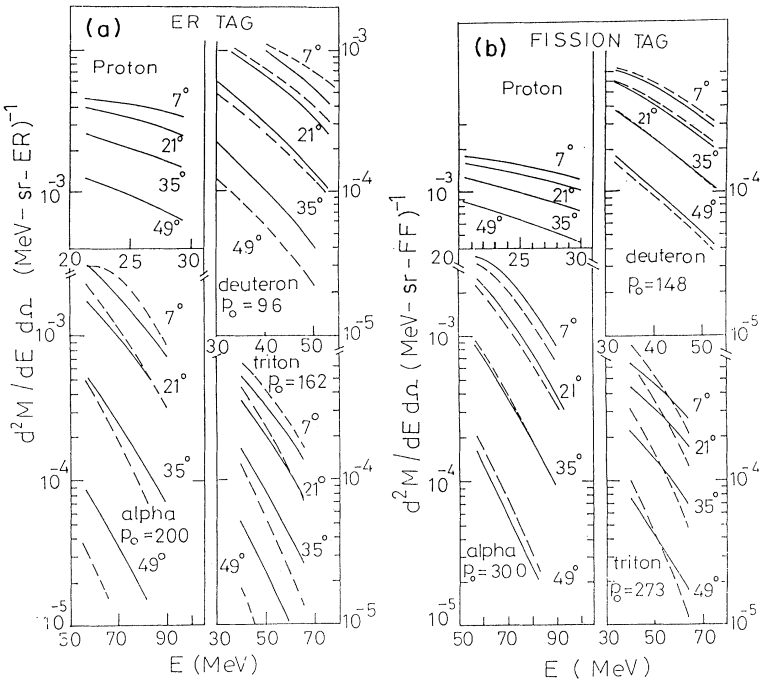

FIG. 17. $\frac{d^2M}{dE\,d\Omega}$ vs E for protons, deuterons, tritons, and alphas in coincidence with (a) evaporation residues and (b) fission. Here the Ta data are presented with the evaporation residue counter is fixed at $\theta = 12°$. The continuous lines represent the moving source fit to the data at angles $\theta = 7°$, 21°, 35°, and 49°. The dashed lines are the coalescence model calculations. The p_0 (MeV/c) values required to fit the complex particle data are also indicated.

Here $E_A = AE - NE_C$ and E_C is the Coulomb repulsion energy per unit charge given as

$$E_C = \frac{(Z_t + Z_p - 1)}{(A_p + A_t - 1)^{1/3}} \text{ MeV}. \quad (15)$$

N_t, N_p, Z_t, Z_p are the neutron and the proton numbers of the target and the projectile, respectively. A_t, A_p are the target and the projectile mass numbers, respectively. Instead of starting from the actual differential multiplicities of the protons measured in this paper, we have taken for convenience the moving source model fitted spectra of protons as starting values in carrying out the coalescence model analysis. We have also assumed uniformly 10% error on the data for all angles and energies in carrying out the analysis. The only parameter which was varied to optimize the fit to complex particle spectra was the quantity p_0 [Eq. (11)]. During the course of the analysis it was found that making $E_C = 0.75E_C$ [as given by Eq. (12)] gave a better fit to the data. This new value of E_C has been used throughout the analysis. The results of the analysis for the composite particle spectra from fission tag and evaporation residue tag are shown in Fig. 17. The overall agreement between the experimental data and the coalescence model calculation can be considered satisfactory considering the simplicity of the model used. The p_0 values determined are listed in Table VI. It is estimated that the errors on these values vary between 10 and 15%. The p_0 values for ^{197}Au and 132 (d), 240 (t), and 279 (α) MeV/c obtained here compare favorably well with the corresponding values 168, 213, and 299 MeV/c determined for the same target at comparable energies in Ref. [1]. In general the p_0 values determined here are consistent with the values obtained in the literature [14, 1, 34] at comparable E/A values of projectiles. There is a tendency for the p_0 values to decrease with increase of A_t. It may be noted from the values tabulated (Table VI) that the p_0 values from evaporation residue tag are considerably smaller than that obtained from fission tag. This result implies that the coalescence radius p_0 is impact parameter dependent.

E. Other models

Tricoire [35] has proposed a promptly emitted particle model for alpha particles similar to that for nucleons discussed above. It is assumed that alpha particles preexist and flow between the projectile and target. Scattering in the receptor is neglected. A schematic version gives an alpha-to-proton ratio depending on the ratio of Fermi velocities (the "Fermi energy" for alphas is taken to be about 3 times that for protons) and independent of impact parameter.

TABLE VI. P_0 (MeV/c) values from coalescence model analysis.

	Fission tag		
	d	t	α
^{159}Tb	150	288	312
^{181}Ta	148	273	300
^{197}Au	132	240	279
	Evaporation residue tag		
	d	t	α
^{159}Tb	114	197	235
^{181}Ta	96	162	200

It would be desirable to have a more sophisticated calculation for the complex particles, such as one based on three-nucleon collisions in a Boltzmann-Uehling-Uhlenbeck transport model [37, 38] or based on "quantum" molecular dynamics [36] to compare with the experimental data.

VII. SUMMARY

We have measured exclusive energy spectra and angular distributions for light charged particles in the forward direction. Impact parameter selection within the class of fusionlike events has been performed by a method which is not compromised by correlation effects arising from conservation laws relating to the observable and the tag. The forward angle spectra are dominated by particles originating from a source with approximately 1/2 to 2/3 the projectile velocity, with the source velocity depending on the parametrization of the spectra in the moving source. The source velocities and energy spectra slope parameters are similar for all the light particles studied. The energy and angle integrated multiplicities associated with this source have been extracted. The proton multiplicity increases almost a factor of 3 with decreasing impact parameter over the range of fusionlike impact parameters, and this dependence is in good agreement with an extended version [30] of a nucleon transport model [12]. The complex particle multiplicities exhibit a different dependence on impact parameter, with the complex particle to proton multiplicity ratio decreasing with decreasing impact parameter. This dependence is not consistent with simple coalescence concepts.

ACKNOWLEDGMENTS

We thank Kenneth Swartz for his assistance during the early stages of this experiment. The work was supported in part by the U.S. Department of Energy.

APPENDIX A: PHOSWICH DETECTOR SYSTEM

1. Mechanical setup

A phoswich detector consists of a thin scintillator acting as a δE counter attached to a thicker scintillator acting as an energy counter, both viewed by a single photomultiplier tube (PMT) attached to the back. The δE versus E measurement allows one to identify particle types. Using a single PMT allows one to pack the detectors close together. An individual detector presents a square face to a particle coming from the target. Each detector is 44.45 cm from the target and is 5.41 cm (or 6.96°) wide. Nearest the target is a 0.036-cm-thick scintillator (Bicron BC400) with a short time constant (1.8 ns) acting as a δE counter. Behind this is a 2.54-cm-thick scintillator (BC444) with a long time constant (180 ns) used to measure the particle energy. Next is a Lucite light guide (to decrease position sensitivity of light collection efficiency) and then the PMT. The BC444 is tapered so that its edges project back to the target. A particle depositing energy in the counter gives rise to a "fast" pulse (due to the thin scintillator) on top of a much longer "slow" pulse (from the thick scintillator). The minimum energy to make it through the thin scintillator is 6 MeV for protons and 24 MeV for alphas. The energy to punch through the thick scintillator is about 55 MeV for protons and 220 MeV for alphas.

The phoswich detectors are held in a support placed in a 152.4-cm-diameter scattering chamber. There are 13 positions in the reaction plane, 5 positions 7° above the reaction plane, and 3 positions 14° above the reaction plane. This support can be placed at virtually any angle from the beam. For the experiments reported here there were 8 in-plane detectors centered at angles of 7°, 14°, 21°, 28°, 35°, 42°, 49°, and 62° and 4 out-of-plane detectors at angles from 7° to 20°. To reduce pile-up due to elastically scattered beam the phoswich counters closest to the beam were covered with 0.013 cm thick tantalum foils. This was thick enough to range out the beam, but thin enough so the particle identification thresholds were only slightly raised, to about 9 MeV for protons and 35 MeV for alphas.

2. Electronics

We sent one anode signal from each of the phoswich counters to the counting room. This was split in three using a Phillips 740 linear fan-out. Two of the outputs were sent to charge sensitive analog-to-digital converters (ADC) to measure the charge in the "fast" and "slow" components. The third signal was used as a timing signal to set up the ADC gates and stop the time-to-digital (TDC) channel.

The analog signal used to measure the fast component was delayed and sent to a LeCroy 2249SG separate gate charge sensitive ADC. The delay was to give the timing electronics enough time to create a 20-ns wide gate and have it arrive at the ADC in coincidence with the fast component of the signal. The separate gates for each of the analog inputs were used to minimize the effect of timing differences between the different phoswich channels.

The analog signal used to measure the slow component was attenuated and sent to a LeCroy 2249A charge sensitive ADC. The gate was 200 ns wide and delayed so the gate started 100 ns after the fast component of the signal. The attenuation was such that the signals of interest did not overflow the ADC range. In the experiment reported here the signal from He overflowed the ADC at an energy of about 110 MeV. None of the $Z = 1$ isotopes came close to overflow.

The timing signal was sent through a Phillips 715 constant fraction discriminator to create a logic signal. One of the outputs was sent to a logical fan-in to create the slow gate common to all the phoswich counters. The other signal was sent to a Phillips 752 logic unit to create two double NIM height signals. One of these signals was used as the fast gate (the LeCroy 2249SG requires a double NIM height gate) and the other was sent through 400 ns of delay cable and used as the TDC stop.

A trigger was defined to be either the FF detector or

ER telescope firing. The phoswich electronics was faster than the surface barrier detectors, so the phoswich signals would arrive before the trigger. If there was no trigger within 5 μs of the phoswich gates the LeCroy ADC's were cleared and reset. The clear time was 2 μs. If there was a trigger the ADC's were allowed to finish conversion and then read. This took approximately 200 μs. The resetting of the phoswich ADC's introduced a 2% dead time. The TDC stops were delayed long enough so the start could be generated by the trigger and timed to the beam marker. The TDC dead time was the same as the surface barrier detectors dead time. Events in which the TDC and ADC information did not match were used to measure the ADC dead time.

3. Calibration

The purpose of the calibration is to use fast, slow, and TOF to identify particle types, then use slow to determine the particle energy.

The fast and slow ADC counts are first corrected for pedestal. The measured number of ADC counts is assumed to be proportional to the light output of the plastic scintillator. The correspondence between light output and energy of the incident particle is made using Birks' formula [39]

$$\frac{dC_{\rm slow}}{dx} = \Lambda_1 \frac{dE/dx}{1+\Lambda_2 dE/dx}. \tag{A1}$$

C is the measured charge in the slow gate and Λ_1 and Λ_2 are calibration constants which are independent of particle type. Λ_1 is a function of the PMT gain and is different for every counter (although the high voltage was set so all counters had similar gains). Λ_2 is a property of the plastic scintillator and takes into account the nonlinearity of the light output for low energy particles. Λ_2 was fixed to be the same for all counters. The measured fast has a contribution from the slow component:

$$\frac{dC_{\rm fast}}{dx} = \Lambda_3 \frac{dE/dx}{1+\Lambda_2 dE/dx} + \Lambda_4 \frac{dC_{\rm slow}}{dx}. \tag{A2}$$

We used three kinds of calibration data. First we elastically scattered beams of protons and He from Au. This gave us a few energy points in each phoswich counter. For protons we had runs up to 18 MeV. For He the highest energy we ran was 64 MeV. During this calibration we did not measure TOF.

The second type of calibration data was taken by placing a Mylar target in the ^{16}O beam. The protons kicked out of the target have energies dependant upon detection angle, ranging from 44 MeV for the forward counters to 22 MeV for the counter at 62°. We also measured TOF during these runs so we could calibrate the TDC's.

The final calibration data were protons and alphas selected from the experimental data using banana gates on fast versus slow. We used the TOF to determine the energy.

To determine Λ_1, Λ_2, Λ_3, and Λ_4 we numerically minimized the quantity

$$\chi^2 = \sum_i \left(\frac{C^i_{\rm slow} - \bar{C}^i_{\rm slow}}{\sigma_{C_{\rm slow}}} \right)^2 + \left(\frac{C^i_{\rm fast} - \bar{C}^i_{\rm fast}}{\sigma_{C_{\rm fast}}} \right)^2, \tag{A3}$$

where $C^i_{\rm slow}$ is the measured number of ADC counts and $\bar{C}^i_{\rm slow}$ is the calculated number of ADC counts. $\bar{C}^i_{\rm slow}$ and $\bar{C}^i_{\rm fast}$ are calculated by numerically integrating Eqs. (A1) and (A2):

$$\bar{C}^i_{\rm slow}(E) = \Lambda_1 \int_{E_2}^{0} \frac{dE'}{1+\Lambda_2 \frac{dE'}{dx}}, \tag{A4}$$

$$\bar{C}^i_{\rm fast}(E) = \Lambda_3 \int_{E_1}^{E_2} \frac{dE'}{1+\Lambda_2 \frac{dE'}{dx}} + \Lambda_4 C^i_{\rm slow}(E). \tag{A5}$$

Here dE'/dx is a function of E' and particle type. The limits of the integrals are the entry and exit energies of the particles. Here we have assumed the particle stops in the slow plastic and it leaves the fast plastic with energy E_2. For the counters covered with a Ta shield we must correct the initial particle energy, E_1, for $\frac{dE}{dx}$ energy loss in the Ta.

4. Particle identification

It is easy to distinguish $Z = 1$ from $Z = 2$. We can combine all phoswich counters in the same plot by plotting

$$I_{\rm slow} = \frac{C_{\rm slow}}{\Lambda_1}, \tag{A6}$$

$$I_{\rm fast} = \frac{C_{\rm fast} - \Lambda_4 C_{\rm slow}}{\Lambda_3}. \tag{A7}$$

An example of such a particle identification scatter plot is shown in Fig. 2. Although the $Z = 1$ and 2 particles are clearly separated, the particle resolution is inadequate to cleanly resolve the p, d, and t particles.

To separate the $Z = 1$ isotopes we use a combination of $\Delta_{\rm fast}$ and $\Delta_{\rm TOF}$, where $\Delta_{\rm fast} = C^{\rm meas}_{\rm fast} - C_{\rm fast}(C^{\rm meas}_{\rm slow})$ is the difference between the measured and expected fast based on the slow component and $\Delta_{\rm TOF} = {\rm TOF}^{\rm meas} - {\rm TOF}(C^{\rm meas}_{\rm slow})$ is the difference between the measured time of flight and the time of flight expected based on the slow component. The plot of $\Delta_{\rm fast}$ versus $\Delta_{\rm TOF}$ for the $Z = 1$ isotopes is shown in Fig. 3. The projection onto the $\Delta_{\rm TOF}$ axis is shown in Fig. 4. The particle identification is somewhat better than is apparent in Fig. 4 as the actual cuts were made in the two-dimensional space of Fig. 3. The p-d separation is quite good, there is an overlap between the d and t isotopes.

The particle energies are deduced from the slow (E) signal. First the particle type is identified, then the energy deposited in the slow plastic is determined by solving Eq. (A4) for E. Finally the particle energy is corrected for dE/dx energy loss in the fast plastic and Ta cover foil (if any).

APPENDIX B: MONTE CARLO CALCULATIONS

The Monte Carlo simulation served two purposes. The first was to check the analysis routines. The second was to calculate the efficiencies necessary for the analysis of the ER tagged data.

1. Monte Carlo simulation of fission fragment tagged data

To check the analysis of the FF tagged data it was only necessary to generate LCP's distributed according to a moving source parametrization.

We chose a set of moving source parameters: multiplicity, source velocity, temperature, and Coulomb barrier. For each event a set of LCP's was generated. The number of a given species of LCP was generated according to a Poisson distribution, with the mean equal to the chosen multiplicity. For each LCP in the event the energy was generated according to a Maxwell-Boltzmann distribution of the given temperature. All LCP's had the Coulomb energy added, and were then boosted along the beam direction by the source velocity. LCP's which were headed toward a phoswich counter were "detected" and added to the appropriate histogram. The result of this program was a set of histograms with the same format as the data. Since the FF detection efficiency is assumed to be independent of the LCP detection efficiency, we assume all FF's are detected.

The generated histograms were fitted with the same fitting program that was used for the data. The fit results were in good agreement with the inputs to the Monte Carlo event generation.

2. Monte Carlo simulation of evaporation residue tagged data

The essential difference between the FF tagged data and the ER tagged data is the correlation between the LCP's and the ER. It is important that we include the ER detection in the Monte Carlo calculation.

There are four processes that we apply to the ER's. Initially we assume full momentum transfer from the beam to the compound nucleus. The first step is to apply momentum conservation to calculate the recoil of the compound nucleus from the LCP's. In the second step we account for the equilibrium evaporation from the hot compound nucleus. The third step is to apply multiple Coulomb scattering and $\frac{dE}{dx}$ on passage through the target. Finally we require the ER to be heading toward the detector and have a kinetic energy above the detector threshold.

We generate the LCP's as before. The ER momentum is just the beam momentum minus the LCP momentum. The charge (Z_{ER}) and mass number (A_{ER}) of the compound nucleus are also corrected for LCP emission.

We use the results of PACE [20] calculations to model the effects of the equilibrium evaporation. Those calculations show the angular deflections due to equilibrium evaporation from the compound nucleus are well described by

$$\frac{d\sigma}{d\Omega} = \frac{1}{\sqrt{2\pi}5.3^\circ} \exp\left[-\frac{1}{2}\left(\frac{\theta}{5.3^\circ}\right)^2\right], \tag{B1}$$

where θ is the change in angle of the ER. The energy of the ER is also modified by the equilibrium evaporation. To a good approximation the ER energy is reduced by 5% with a Gaussian distribution about this mean described by $\sigma = 0.15E_{\mathrm{ER}}$. The mass number of the compound nucleus is also reduced by five, the average number of neutrons emitted.

The dE/dx energy loss of the ER in the passage through the target is parametrized as

$$dE = 20t\left[\frac{E_{\mathrm{ER}}}{A_{\mathrm{ER}}}\right]^{0.66}, \tag{B2}$$

where t is the target thickness and A_{ER} is the mass number of the ER. This reproduces the dE/dx values tabulated in the Nuclear Data Tables for our energy range [40]. The multiple Coulomb scattering is difficult to parametrize; we have scattering angles past the Gaussian approximation and the target is too thick for Rutherford scattering to be applicable. We use tabulated values of $\frac{d\sigma}{d\Omega}$ for multiple Coulomb scattering published by Sigmund and Winterbon [41] and assume one-half the target thickness as the average amount of material for multiple scattering.

In the final step we define a "trigger" if the ER is above the detector energy threshold and it is heading toward the detector. The number of triggers divided by the number of attempts is the tag efficiency ϵ_{ER}. For all triggered events we check if any of the LCP's were detected in the phoswich array. We again accumulate histograms so the results of the Monte Carlo run are in the same format as the data and can be analyzed with the same programs.

The calculation of $\epsilon_{\mathrm{ER-phos}}(E,p)$ is a little different than the calculation of ϵ_{ER}. The essential difference is in the generation of the LCP's. For each LCP species we loop over phoswich counters, then over LCP energy, generating an LCP of the given type and energy into a random spot on the phoswich counter. The recoil of the ER from this LCP is calculated as described before. The fraction of events in which the ER is detected divided by the number of events generated is $\epsilon_{\mathrm{ER-phos}}(E,p)/\Omega_{\mathrm{phos}}$.

Generating enough events to get adequate statistics on $\epsilon_{\mathrm{ER-phos}}(E,p)$ was quite time consuming. We reduced the time consumption by calculating $\epsilon_{\mathrm{ER-phos}}(E,p)$ every few MeV and using a polynomial fit to fill in the gaps and smooth the calculation.

[1] T.C. Awes *et al.*, Phys. Rev. C **25**, 2361 (1982).
[2] E. Holub, D. Hilscher, G. Ingold, U. Jahnke, H. Orf, and R. Rossner, Phys. Rev. C **28**, 252 (1983).
[3] M. Bini *et al.*, Phys. Rev. C **22**, 1945 (1980).
[4] G.R. Young, R.L. Ferguson, A. Gavron, D.C. Hensley, F.E. Obershain, F. Plasil, A.H. Snell, M.P. Webb, C.F. Maguire, and G.A. Petit, Phys. Rev. C **45**, 1389 (1980).
[5] H. Homeyer, M. Bürgel, M. Clover, Ch. Egelhaaf, H. Fuchs, A. Gamp, D. Kovar, and W. Rauch, Phys. Rev. C **26**, 1335 (1982).
[6] J.C. Steckmeyer *et al.*, Nucl. Phys. **A500**, 372 (1989).
[7] J. Pouliot *et al.*, Phys. Lett. B **223**, 16 (1989).
[8] J.P. Bondorf *et al.*, Nucl. Phys. **A333**, 285 (1980).
[9] F. Sebille and B. Remaud, Z. Phys. A **310**, 99 (1983).
[10] R. Vandenbosch, in *Nuclear Physics with Heavy Ions; Prospects at Energies Below 20 MeV/amu*, edited by P. Braun-Munzinger (Harwood Academic, New York, 1984), p. 447.
[11] S. Leray *et al.*, Z. Phys. A **320**, 383 (1985).
[12] J. Randrup and R. Vandenbosch, Nucl. Phys. **A474**, 219 (1987).
[13] S. Bhattacharya, K. Krishan, S.K. Samaddar, and J.N. De, Phys. Rev. C **37**, 2916 (1988).
[14] T.C. Awes *et al.*, Phys. Rev. C **24**, 89 (1981).
[15] M.B. Tsang, G.F. Bertsch, W.G. Lynch, and M. Tokyama, Phys. Rev. C **40**, 1685 (1989).
[16] J. Peter *et al.*, Phys. Lett. B **237**, 187 (1990).
[17] L.C. Vaz, D. Logan, E. Duek, J.M. Alexander, M.F. Rivet, M.S. Zisman, M. Kaplan, and J.W. Ball, Z. Phys. **315**, 169 (1984).
[18] A. Gavron *et al.*, Phys. Rev. C **30**, 1552 (1984).
[19] V. Viola *et al.*, Phys. Rev. C **26**, 180 (1982).
[20] A. Gavron, Phys. Rev. C **21**, 230 (1981).
[21] M. Thoenessen and J.R. Beene, Phys. Rev. C **45**, 873 (1992).
[22] R. Wada *et al.*, Phys. Rev. C **39**, 497 (1989).
[23] M.B. Tsang, C.B. Chitwood, D.J. Fields, C.K. Gelbke, D.R. Klesch, W.G. Lynch, K. Kwiatkowski, and V.E. Viola, Jr., Phys. Rev. Lett. **52**, 1907 (1984).
[24] M.B. Tsang *et al.*, Phys. Rev. C **42**, R15 (1990).
[25] T. Ethvignot *et al.*, Phys. Rev. C **43**, R2035 (1991).
[26] M.B. Tsang, R.T. de Souza, Y.D. Kim, D.R. Bowman, N. Carlin, C.K. Gelbke, W.G. Gong, W.E. Lynch, L. Phair, and F. Zhu, Phys. Rev. C **44**, 2065 (1991).
[27] D. Jouan, B. Borderie, M.F. Rivet, C. Cabot, H. Fuch, H. Gauvin, C. Gregoire, F. Hanappe, D. Gardes, M. Montoya, B. Remaud, and F. Sebille, Z. Phys. A **340**, 63 (1992).
[28] K.A. Griffioen, B.J. Gluckman, R.J. Meijer, P. Decowski, and R. Kamermans, Phys. Rev. C **40**, 1647 (1989).
[29] H.K.W. Leegte, A.L. Boonstra, J.D. Hinnefeld, E.E. Koldenhof, R.H. Siemssen, K. Siwek-Wilczynska, Z. Sosin, J. Wilczynski, and H.W. Wilschut, Phys. Rev. C **46**, 991 (1992).
[30] S.J. Luke, Ph.D. thesis.
[31] S.J. Luke, R. Vandenbosch, and J. Randrup, Phys. Rev. C (to be published).
[32] S. Datta, R. Caplan, N. Cindro, R.L. Auble, J.B. Ball, and R.L. Robinson, Phys. Lett. B **192**, 302 (1989).
[33] S. Datta, R. Caplan, N. Cindro, R.L. Auble, J.B. Ball, and R.L. Robinson, J. Phys. G. **14**, 937 (1988).
[34] T. Fukada, M. Ishihara, H. Ogata, I. Miura, T. Shimoda, K. Katori, S. Shimoura, M.K. Tanaka, E. Takada, and T. Otsuka, Nucl. Phys. **A425**, 548 (1984).
[35] H. Tricoire, Z. Phys. A **312**, 221 (1983).
[36] J. Aichelin and H. Stocker, Phys. Lett. B **176**, 14 (1986).
[37] P. Danielewicz and G.F. Bertsch, Nucl. Phys. **A533**, 712 (1991).
[38] M.B. Tsang, P. Danielewicz, D.R. Bowman, N. Carlin, C.K. Gelbke, Y.D. Kim, W.G. Lynch, L. Phair, R.T. de Souza, and F. Zhu, Phys. Lett. B **297**, 243 (1993).
[39] J.B. Birks, *Scintillation Counters* (McGraw-Hill, New York, 1953).
[40] At. Data Nucl. Data Tables **29**, 1 (1983).
[41] P. Sigmund and K. B. Winterbon, Nucl. Instrum. Methods **119**, 541 (1974).

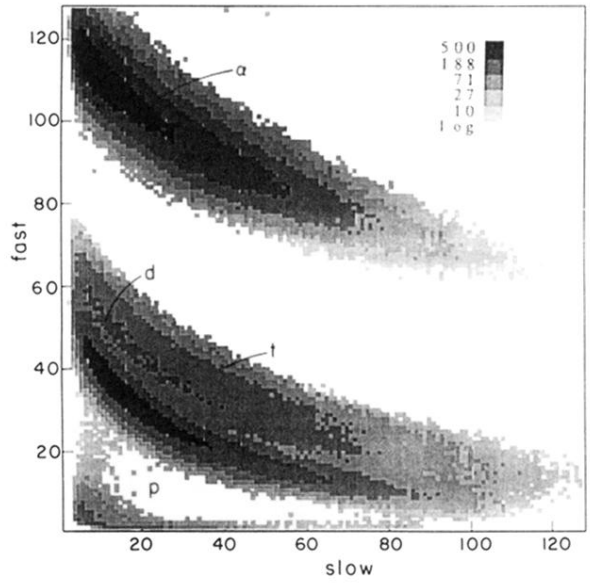

FIG. 2. δE vs E. "Fast" (dE) component of phoswich signal is vertical axis and "slow" (E) component of phoswich signal is horizontal axis. The gradation of the grey scale is logarithmic. The measured ADC values have been corrected for pedestals and then scaled to a uniform PMT gain. See Sec. III A for more details on the scaling.

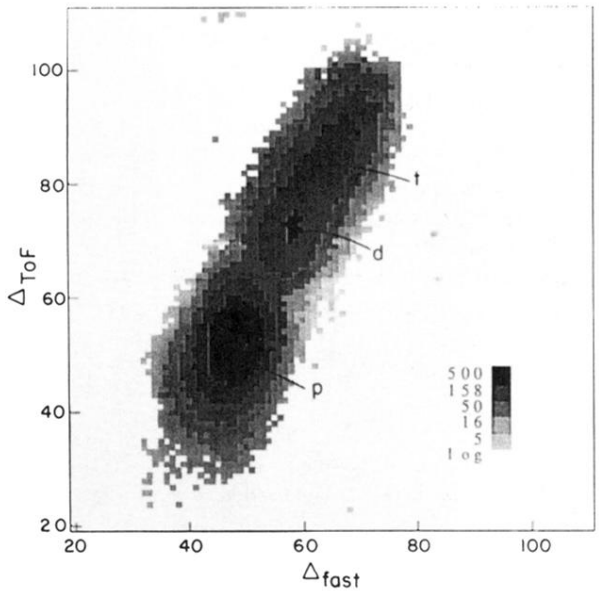

FIG. 3. Δ_{fast} (x axis) vs Δ_{TOF} (y axis) for $Z = 1$. Δ_{fast} is the measured "fast" minus the "fast" expected from protons Δ_{TOF} is the measured time of flight (TOF) minus the TOF expected for protons.

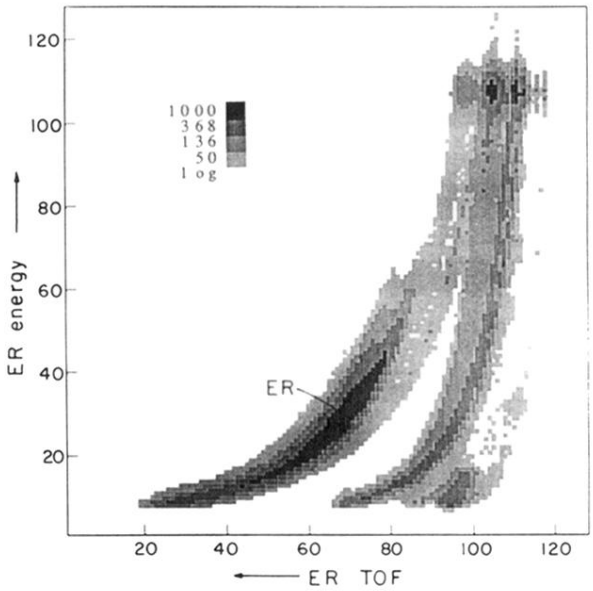

FIG. 5. Evaporation residue energy vs time of flight (TOF) scatter plot. The vertical axis is the measured pulse height. TOF increases from right to left along the horizontal axis.